

Novel Hierarchical Ni/MgO Catalyst for Highly Efficient CO Methanation in a Fluidized Bed Reactor

Jun Li and Qingshan Zhu

State Key Laboratory of Multiphase Complex Systems, Institute of Process Engineering, Chinese Academy of Sciences, Beijing 100190, China

Wencai Peng, Qiang Zhang, Guohua Luo, and Fei Wei

Beijing Key Laboratory of Green Chemical Reaction Engineering and Technology, Dept. of Chemical Engineering, Tsinghua University, Beijing 100084, China

DOI 10.1002/aic.15597

Published online January 6, 2017 in Wiley Online Library (wileyonlinelibrary.com)

A facile synthesis of the hierarchical Ni/MgO catalyst is reported, with extremely fine dispersion of Ni nanoparticles (NPs) and high surface oxygen mobility. The hierarchical Ni/MgO catalyst exhibits higher activity for CH₄ formation than that prepared by the impregnation method. The enhanced activity and thermal stability of the hierarchical Ni/MgO catalyst is attributed to hierarchical MgO particles with a multilayer structure and high surface oxygen mobility. This induces better metal-support interactions, high Ni dispersion to prevent Ni NPs sintering, and the high surface oxygen mobility provides a high resistance to carbon deposition. Compared to the impregnated Ni/MgO catalyst, the hierarchical Ni/MgO catalyst exhibits a better fluidization quality and a higher attrition-resistance in a fluidized-bed reactor. This approach to improve the catalytic activity by creation of hierarchical Ni/MgO particles is encouraging for the design of novel catalysts for synthetic natural gas production, especially from the perspective of matching catalysts with fluidized-bed reactors. © 2017 American Institute of Chemical Engineers AICHE J, 63: 2141–2152, 2017

Keywords: hierarchical particles, Ni/MgO, CO methanation, fluidized-bed

Introduction

Natural gas is a highly efficient form of energy and the cleanest fossil fuel by virtue of its high calorific value and smoke- and slag-free combustion properties.¹ Increased demand for natural gas and increasingly strict environmental emission standards have driven the pursuit of feasible approaches for the production of synthetic natural gas (SNG). There are challenges in the gasification of coal for the production of syngas (H₂/CO) and subsequent methanation.^{2,3} CO methanation, as a key reaction during this transformation, is highly exothermic and is accompanied by a large decrease in the number of moles. Thermodynamically, this reaction is favored at low temperatures, but kinetically, it is favored at high temperatures. Heat removal to avoid hot spots, which induce sintering of the active metal and/or support and carbon deposition during the methanation reaction, has been a major concern in industrial methanation processes.^{4–8} Consequently, the major objectives of the development of a methanation reactor are the efficient removal of the heat of reaction from the reactor, to avoid hot spots, and to minimize the deactivation of catalysts. In the case of fixed bed reactors, several reactors connected in series with intermediate cooling gas components or product gas recycling are required to prevent

the formation of hot spots.^{2,9} This mode of operation consumes high amounts of energy and is low in efficiency.

Methanation via fluidized-bed reactors has the advantage of almost isothermal conditions in the reactor due to its superior heat transfer capability. Fluidized-bed methanation reactors have been investigated at a large scale and include the multiple-feed fluidized-bed reactor process,¹⁰ the Bi-Gas project,¹¹ the Comflux process,¹² and the biomass-derived SNG process developed by the Paul Scherrer Institute (PSI).¹³ The biomass-derived SNG process is now available on the market and can be connected to any gasifier.¹⁴ However, the other three fluidized methanation processes were halted due to economical considerations^{11,12} and poor fluidization.¹⁰ In addition to the catalytic activity, the better fluidization quality and attrition-resistance of the catalyst particles play a positive role in fluidized-bed methanation.^{15,16}

Metal nanoparticles (NPs), such as Ru, Rh, Ni, and Co on various supports have been proposed as effective catalysts for methanation.^{17–20} Ru-based catalysts have shown high activity for CO methanation. However, large-scale applications of these catalysts are restricted due to the high cost. Catalysts based on Ni NPs, with relatively high activity, are used extensively in industrial applications. Ni on various supports, such as TiO₂, Al₂O₃, SiO₂, ZrO₂, and SiC,^{1,21–24} has been investigated. It has been demonstrated that the catalytic performance is related to the size and shape of the metal NPs and the metal-support interactions.^{25–27} In general, CO methanation activity is significantly higher for Al₂O₃ supports than for SiO₂

Correspondence concerning this article should be addressed to Q. S. Zhu at qszhu@ipe.ac.cn; F. Wei at wf-dce@tsinghua.edu.cn.

supports.^{28,29} Therefore, Ni supported on Al₂O₃ catalysts has been explored extensively.^{30–32} However, these Ni NPs supported on Al₂O₃ catalysts tend to aggregate together to form a random structure at high temperatures, resulting in rapid deactivation of the catalyst.^{33,34} Further, carbon deposition and the formation of the NiAl₂O₄ phase at high temperature reduce the CO methanation activity.³⁵ Consequently, several chemical approaches, such as anchoring^{36,37} or embedding³⁸ metals onto the support, the formation of core-shell and hollow structures,^{39–41} overcoating,⁴² and alloying,⁴³ have been explored to stabilize metal NPs and to improve the resistance to carbon deposition. MgO was found to be an effective promoter to avoid carbon deposition and to prevent the sintering of Ni particles.³³ However, metals supported on individual MgO particles for catalytic CO methanation have not been fully investigated in the literature, probably due to the low surface area of MgO particles.^{44–46}

In addition, most of the aforementioned catalysts have been developed on the basis of fixed-bed methanation reactors. However, the fluidization quality and attrition strength of the nanosized catalysts in fluidized-bed reactors are critical for obtaining high reactivity and a long lifespan, especially for the highly exothermic methanation reaction accompanied by a large decrease in gas volume.^{3,47–49} Therefore, it is important to develop a highly active catalyst that is not only stable against sintering and carbon deposition but also able to fluidize sufficiently in fluidized-bed reactors.

Herein, we explore the idea of hierarchical particles self-assembled by metal NPs with a high thermal stability and suitable for fluidized CO methanation during SNG production. In this study, the performance of Ni NPs supported on hierarchical MgO particles was investigated for the production of SNG via CO methanation. The hierarchical Ni/MgO catalyst exhibits much higher activity and a stronger resistance to attrition and carbon deposition compared to the catalyst synthesized by the conventional impregnation method.

Experimental Methods

Catalyst preparation

The hierarchical Ni/MgO catalyst was fabricated through a simple hydrothermal precipitation route. In a typical synthesis procedure, Mg(NO₃)₂•6H₂O (AR grade, J&K Corp), Ni(NO₃)₂•6H₂O (AR grade, J&K Corp), and urea (AR grade, J&K Corp) were dissolved in 50.0 mL deionized water with [Mg²⁺] = 0.2 mol/L, n(Ni):n(Mg) = 1:10, n(Urea) = 2.0 mol/L. The solution was poured into a 100 mL Teflon bottle. Subsequently, the Teflon bottle containing this solution was held in a stainless steel autoclave, which was sealed tightly. Then, the autoclave was transferred into a temperature-controlled electric oven and was subjected to hydrothermal treatment at 200°C for 24 h. After the hydrothermal treatment, the solution was cooled to room temperature naturally. The Ni-Mg precursors were obtained after a treatment process consisting of filtration, washing, and drying. Finally, the as-obtained Ni/MgO precursors were calcined at 500°C for 5 h. The as-obtained hierarchical Ni/MgO NPs are denoted as MSP.

For comparison, a Ni/MgO catalyst was prepared by incipiently impregnating the support of MgO NPs with an aqueous solution using Ni(NO₃)₂•6H₂O as the precursor to NiO with a loading of 10 wt %. This was followed by calcination in air at 500°C for 5 h. The sample was designated as IMP.

Catalyst characterizations

The X-ray diffraction (XRD) patterns were recorded on an X-ray diffractometer (XRD, X'Pert MPD Pro, Panalytical, Netherlands) with Cu K_a radiation ($k = 1.5408 \text{ \AA}$) at 40 kV and 40 mA.

The Brunauer-Emmett-Teller (BET) specific surface area, total pore volume, and average pore diameter were determined from N₂ adsorption/desorption isotherms at liquid-N₂ temperature using Micromeritics Flow Sorb II 2300. Before each measurement, the sample was degassed in a vacuum at 300°C for 3 h.

The morphology of the as-synthesized catalysts was characterized using a JSM-7001F (FESEM, JEOL, Japan) scanning electron microscope (SEM) and a JEM-2010F transmission electron microscope (TEM) equipped with an energy dispersive X-ray spectroscopy (EDS) detector (INCA X-Max). The metal particle size was measured using a high-angle annular dark field scanning TEM (HAADF-STEM, JEM ARM200F, JEOL, Japan) operated at 200 kV. The size distributions of metal particles on the catalyst surface were obtained on the basis of statistical analysis of SEM and TEM images.

Tests of H₂-temperature-programmed reduction (TPR) were conducted using a chemisorption apparatus (ChemBet 3000, Quantachrom, USA). The sample (200 mg) was pretreated with a pure He flow at 300°C for 60 min, followed by cooling to room temperature. Then, the sample was heated to 900°C at a constant heating rate of 10°C/min, using a H₂/He flow (5% H₂, vol %) at a rate of 100 mL/min. Changes of the hydrogen signal were monitored by an on-line GC (Shimadzu GC-8A) with a TCD detector.

H₂-temperature-programmed desorption (H₂-TPD) tests were also performed on the Quantachrom ChemBet 3000. Before a H₂-TPD test, the sample (200 mg) was pre-reduced at 600°C for 2 h under a 10% H₂/Ar flow and then for another 90 min in pure Ar to minimize the H₂ spillover. The sample was then cooled down to room temperature, and a H₂-TPD experiment was performed at a heating rate of 10°C/min under a pure Ar flow.

CO₂-TPD was performed on the same Quantachrom ChemBet 3000. Catalyst samples (200 mg) were pretreated at 500°C for 1 h under a pure He flow. After cooling to room temperature in He, 10% CO₂/He adsorption was performed at 80°C for 1 h. The catalysts were then purged with He at a rate of 100 mL/min for 1 h to remove the physisorbed CO₂. The temperature was increased from 80 to 800°C at a rate of 10°C/min under a pure He flow.

The attrition-resistance of the catalysts was evaluated by a modified air-jet attrition test, according to the ASTM method (ASTM D5757-00), which is widely employed to measure the attrition of FCC catalysts. For the attrition test, a 30 g sample of 30–100 μm was placed in an air flow of 9 L/min at room temperature for 4 h. After the test, catalyst particles smaller than 30 μm remaining in the attrition tube and those collected by a thimble filter at the outlet of the settling chamber were defined as fine particles. The attrition index (AI) is defined as follows:

AI (%) = [total fine particles collected in 4 h (g)/initial sample amount (30 g)]/4 × 100%.

Catalyst test

The methanation performance of the catalysts was performed in a fluidized-bed reactor system, including a gas feeding subsystem, a fluidized-bed reactor (i.d. of 16 mm)

Table 1. Physicochemical Properties of the MSP and IMP Catalysts

Catalysts	MSP	IMP
Bulk density (kg/m ³)	1160	600
BET (m ² /g)	225	63.8
Average pore diameter (nm)	9.8	30.2
Metal particle size ^a (nm)	4.8	5.8
Ni dispersion ^b (%)	32.6	11.5
Attrition index (%)	2.5	5.8

^aMetal particle sizes were estimated by TEM.

^bBased on H₂ chemisorption, assuming H_{ad}/Ni_s = 1.

collocated with a heat furnace, and a GC (M3000) analyzer. The bed pressure drop was measured by a differential pressure transducer equipped with high/low pressure ports, which was placed at the bottom of the fluidized-bed reactor. The reactions were tested over the temperature range of 200–500°C. The temperature of the furnace was controlled by a K-type thermocoupler located outside the fluidized-bed reactor, and the temperature of the catalyst bed was also monitored by another K-type thermocoupler inserted in direct contact with the catalyst bed to determine the real temperature of the methanation reaction. The gas hourly space velocity (h⁻¹) was selected to be 30,000 h⁻¹ under atmospheric pressure. The gas velocity (u) was 0.02 m/s under standard conditions (u/u_{mf} = 4).

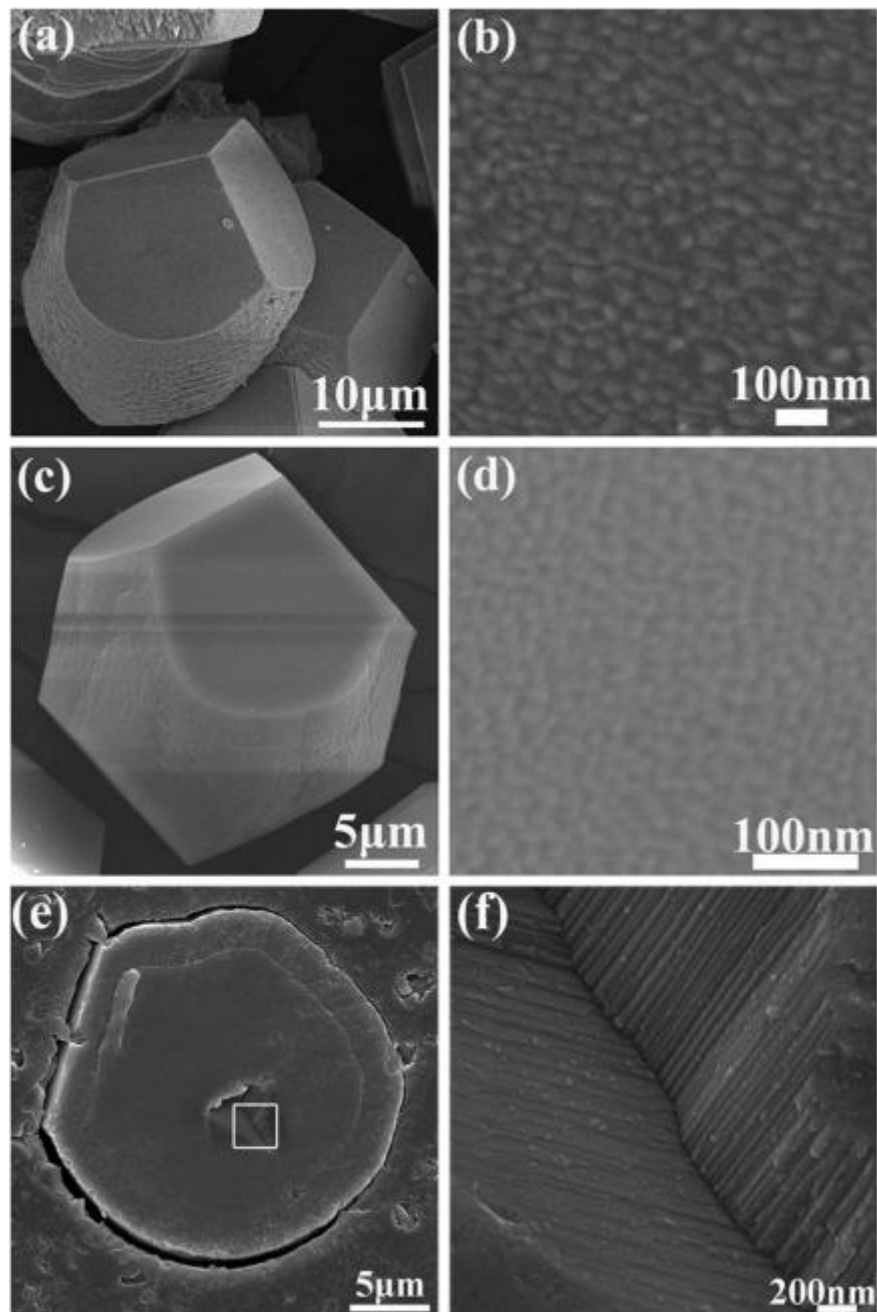


Figure 1. Hierarchical MgO particles (a) and their enlarged SEM image (b), Ni/MgO particles (c) and their enlarged SEM image (d) calcined in air at 500°C for 5 h, (e) cross-sectional map of Ni/MgO NPs and (f) enlarged image of the white region in (e).

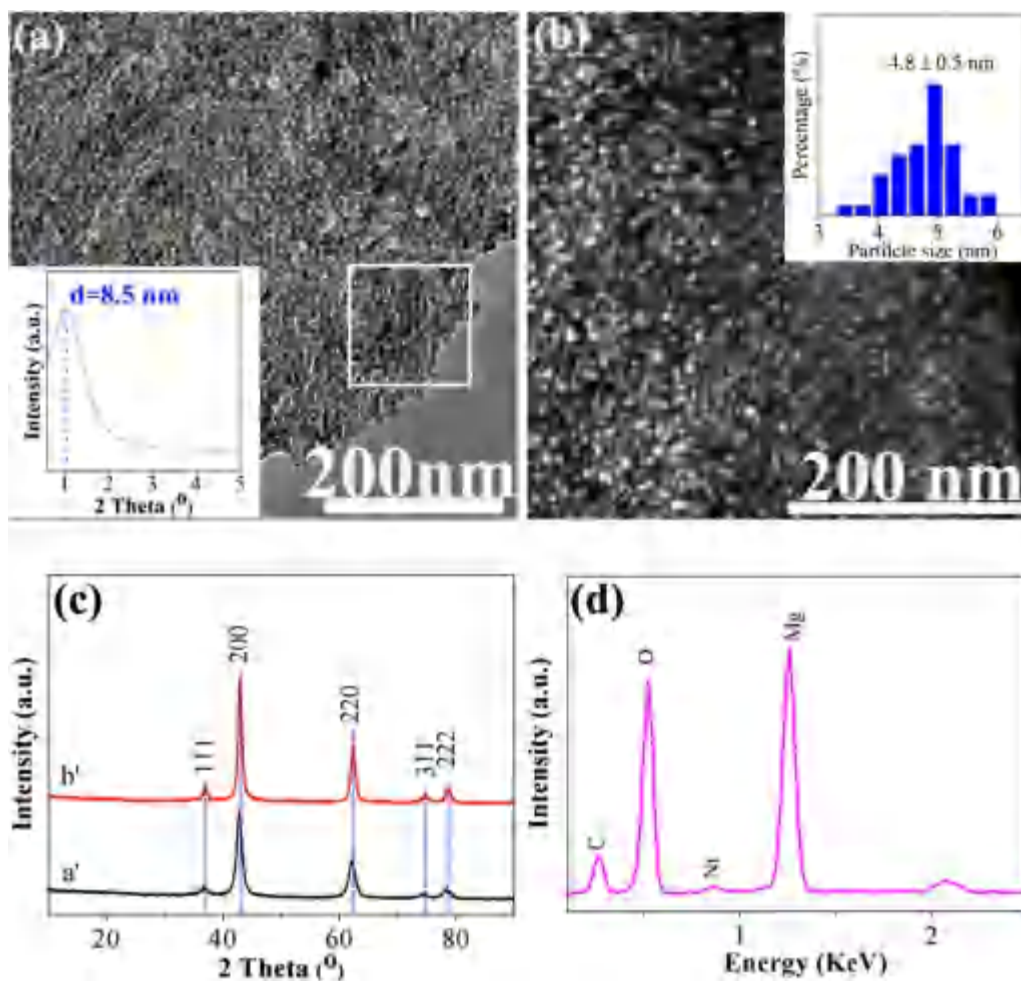


Figure 2. (a) TEM image of Ni/MgO particles calcined at 500°C for 5 h, with the inset showing the small angle XRD pattern of Ni/MgO particles. (b) STEM images of Ni/MgO particles reduced at 600°C for 4 h, with the inset showing the size distribution of Ni NPs. (c) XRD patterns of the Ni-Mg particles calcined at 500°C for 5 h (a') and its form after reduction at 600°C for 4 h (b'). (d) EDX spectra of the white region in (a).

[Color figure can be viewed at wileyonlinelibrary.com]

The particle size of the catalyst was in the range of 25–100 nm, with an average size of 45 nm. For the reaction, 2.0 g of the catalyst particles were loaded into the fluidized-bed reactor with a settled bed height of 9.0 mm for MSP and 16.0 mm for IMP, based on the weight of catalyst loaded and the bulk density in Table 1. Prior to the reaction, the catalyst particles were pre-reduced using H₂ (100 mL/min) at 600°C for 4 h. After the reduction, syngas with CO/H₂/N₂ = 1:3:1 was introduced into the reactor to start the methanation test. The outlet gas stream was cooled by an ice trap. To determine the composition of the outlet gas, the gas product (H₂, N₂, CH₄, CO₂, and CO) was collected after steady-state operation for 0.5 h at each temperature and analyzed by the GC analyzer. The CO conversion, CH₄ selectivity, and yield were calculated as follows:

$$\text{CO conversion : } X_{\text{CO}}(\%) = \frac{V_{\text{CO,in}} - V_{\text{CO,out}}}{V_{\text{CO,in}}} \times 100 \quad (1)$$

$$\text{CH}_4 \text{ selectivity : } S_{\text{CH}_4}(\%) = \frac{V_{\text{CH}_4,\text{out}}}{V_{\text{CO,in}} - V_{\text{CO,out}}} \times 100 \quad (2)$$

$$\text{CH}_4 \text{ yield : } Y_{\text{CH}_4}(\%) = \frac{V_{\text{CH}_4,\text{out}}}{V_{\text{CO,in}}} \times 100 \quad (3)$$

where X is the conversion of CO, S is the selectivity of CH₄, Y is the yield of CH₄, $V_{i,\text{in}}$ (mL/min) and $V_{i,\text{out}}$ (mL/min) are the

inlet and outlet volumetric flow rate of each respective species i ($i = \text{CO}, \text{CO}_2, \text{H}_2, \text{and CH}_4$).

Results and Discussion

Characteristics of hierarchical Ni/MgO catalyst

The hierarchical MgO precursor, synthesized by the hydrothermal precipitation route, was calcined at 500°C for 5 h to remove CO₃²⁻ and OH⁻ and to obtain the hierarchical MgO particles. Individual MgO particles display a pentagonal dodecahedron-like morphology and a multi-layered structure (Figure 1a), formed via self-assembly from many octahedral nano-crystals (Figure 1b). This hierarchical structure is still well-preserved after the introduction of Ni²⁺ into the MgO nano-crystals (Figures 1c–d). The cross-section of the structure of Ni/MgO particles was also characterized using a JSM-7001F (FESEM, JEOL, Japan) SEM, as shown in Figure 1e. Figure 1f shows the enlarged image of the boxed area in Figure 1e. It can be observed that the Ni/MgO particles consist of multilayer structures.

The NiO/MgO particles exhibit a high porosity with a short-range ordered mesoporous structure, as shown by the TEM image in Figure 2a. The strong diffraction peak at approximately 1.03° ($d = 8.5$ nm), as characterized by the small-angle

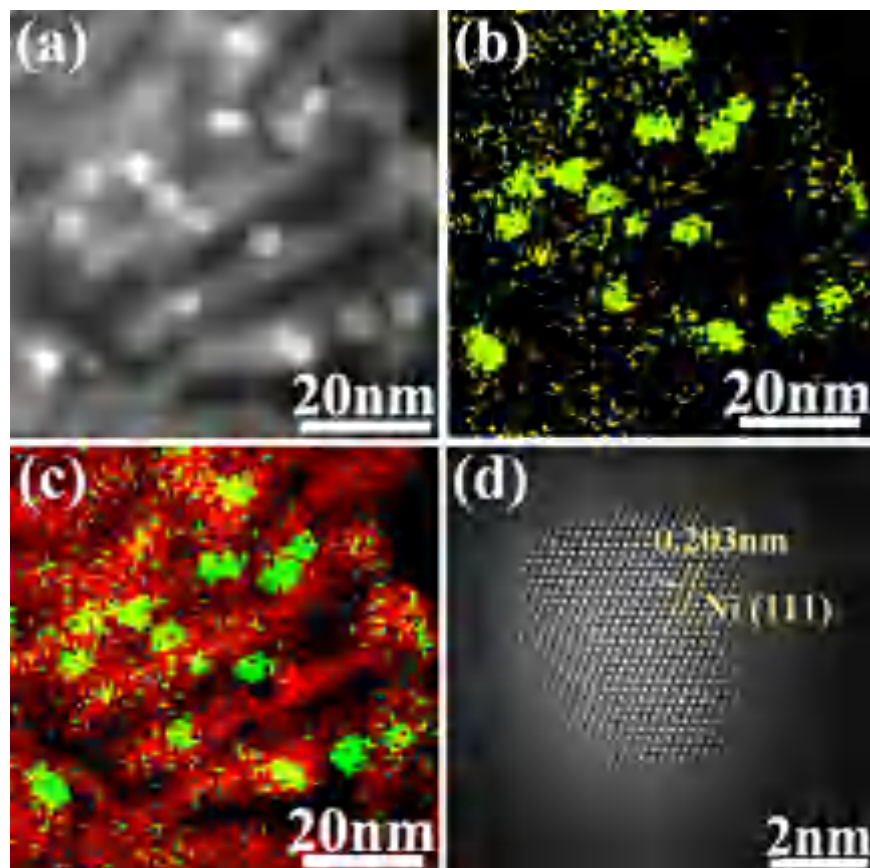


Figure 3. High-angle annular dark-field (HAADF)-STEM image (a), Ni map (b), Ni-Mg mixed map (c), and Ni nanocrystals (d) of the Ni NPs embedded on MgO nanoparticles reduced at 600°C for 4 h.

[Color figure can be viewed at wileyonlinelibrary.com]

XRD pattern (Figure 2a, insert), shows the formation of mesostructures, which is consistent with the TEM observations. The powder XRD data (Figure 2c, a') shows only peaks for MgO with good crystallinity and no other lines from Ni-containing phases. However, the EDX spectra in Figure 2d indicate that the Ni/MgO particles consist of 5% Ni, 41% Mg, and 49% O by atomic ratio. These findings indicate unambiguously the formation of the NiO-MgO solid solution. When the NiO/MgO particles were subjected to H₂ reduction at 600°C for 4 h, no phase from metallic nickel was detected (Figure 2c, b'), indicating that the Ni NPs are extremely small and well-dispersed on the MgO layers. This is also confirmed by the STEM image that shows well-dispersed Ni nanocrystals (Figure 2b) with particles sizes of 3–6 nm (mean = 4.8 nm) (Figure 2b, insert).

Figure 3a shows STEM images of Ni nanocrystals on the hierarchical MgO particles. The Ni NPs are very small and embedded on the hierarchical MgO particles. The Ni EDS mapping results reveal that there are Mg elements around the Ni NPs. This indicates that the Mg elements are pinned between the Ni NPs to prevent further sintering of the Ni NPs (Figures 3b–c). The STEM image in Figure 3d shows that the individual Ni crystal is piled by Ni atoms in the rhombic form, with an angle of 108°. The exposed face of the Ni crystal is the Ni (111) face, which is undoubtedly active in the catalytic reaction.⁴⁴

The N₂-isothermal adsorption-desorption and pore size distribution (BJH method) curves of Ni-Mg particles are illustrated in Figure 4. The nitrogen adsorption-desorption isotherm

exhibits a type IV curve with an H1-shaped hysteresis loop, suggesting that the mesopores are uniform (Figure 4a). The pore size distribution curve indicates an extraordinarily narrow pore-size distribution centered at 9.8 nm (Figure 4b). The average thickness of the MgO layer was estimated from the TEM characterization to be ca. 6.1 nm, which is likely beneficial for full exposure of the active sites.

The BJH pore diameter and the specific BET surface area as well as the metal size and dispersion are summarized in Table 1. It is clear that MSP has a large BET surface area of 225 m²/g and a high Ni dispersal of 32.6%. The BET surface area of MSP is much greater than those of NiO-MgO catalysts reported previously.^{8,45,46,50–55} This is attributed to the multi-layer structure of MgO, with its highly-corrugated surfaces. The greater dispersal of Ni may be attributable to better contact with the MgO support, which was further corroborated by the TPR analyses. Figure 5 shows the H₂-TPR profiles of the MSP and IMP catalysts. According to previous reports,⁵⁵ the reducible NiO species are classified into three types: (1) a surface “NiO-rich” MgO-NiO solid solution reducible in the low-temperature region of 200–600°C; (2) a surface “MgO-rich” NiO-MgO solid solution reducible in the high-temperature region of 600–1000°C; and (3) a “bulk” NiO-MgO solid solution, reducible at temperatures higher than 1000°C. As observed in Figure 5, the IMP catalyst shows a wide range of reduction peaks at 747.5°C, indicating the difficulty of reduction. However, the MSP catalyst exhibits a significantly centralized reduction peak at 547.7°C, implying the high dispersion of Ni NPs. Compared to the IMP catalyst, the MSP

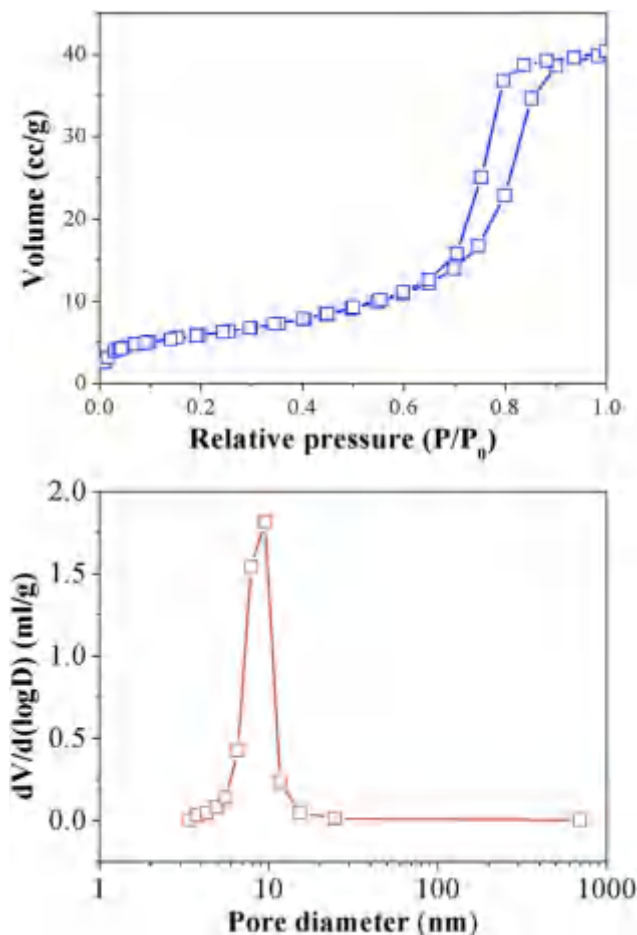


Figure 4. Isothermal adsorption-desorption curves (a) and pore size distribution (b) of Ni-Mg particles.

[Color figure can be viewed at wileyonlinelibrary.com]

catalyst is much more abundant in “MgO-rich” NiO-MgO species. The NiO in such species was easy to reduce at 600°C, probably contributing to its high Ni dispersion.³³

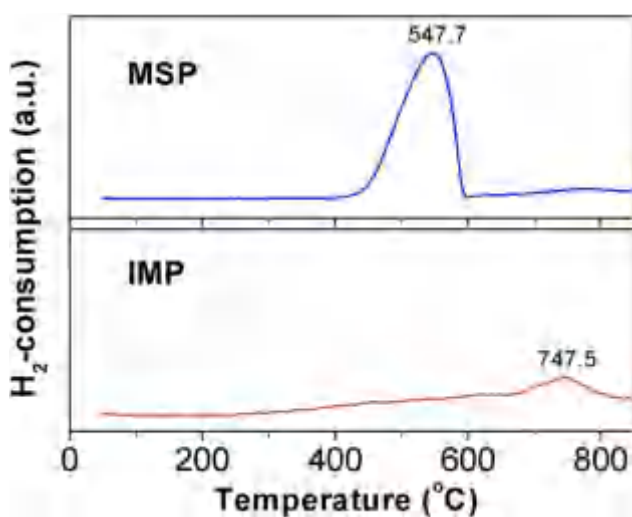


Figure 5. H₂-TPR profiles of a hierarchical Ni/MgO catalyst (MSP) and conventional impregnated Ni/MgO (IMP) catalysts.

[Color figure can be viewed at wileyonlinelibrary.com]

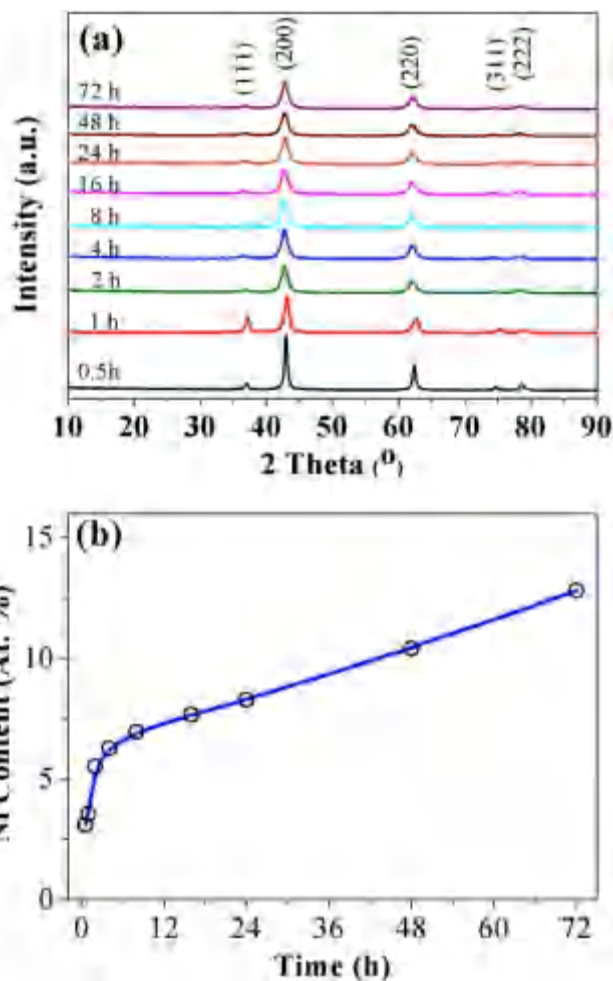


Figure 6. XRD patterns (a) and Ni content (b) of the Ni/MgO NPs obtained after different hydrothermal treatment times at 200°C and calcination at 500°C for 5 h.

[Color figure can be viewed at wileyonlinelibrary.com]

To elucidate the formation mechanism of Ni NPs on MgO particles, Ni NPs obtained after different durations of hydrothermal treatment were analyzed by XRD, SEM, and EDS. No peak for the NiO phase is detected, while only MgO diffraction peaks are observed on the Ni-MgO catalysts (Figure 6a). The (200) peaks of MgO shift to a lower angle, and the (111) peaks of MgO show an apparent decrease with increasing duration of hydrothermal treatment, indicating that nickel oxide is incorporated into the MgO lattice by replacing the Mg atoms in the (111) crystal face, thus forming a surface “MgO-rich” NiO-MgO solid solution. This agrees well with the result of Figure 3d. Correspondingly, the Ni content increases continually with increasing duration of hydrothermal treatment (Figure 6b).

Catalytic performance

The evaluation of initial catalytic activity of the hierarchical Ni/MgO (MSP) and impregnated Ni/MgO (IMP) catalysts was conducted in the fluidized-bed reactor. After the introduction of syngas (CO and H₂), the MSP exhibited a high CO conversion and high selectivity and yield of CH₄, with values very close to the thermodynamic equilibrium values in the temperature range of 350–500°C (Figure 7a). However, when the

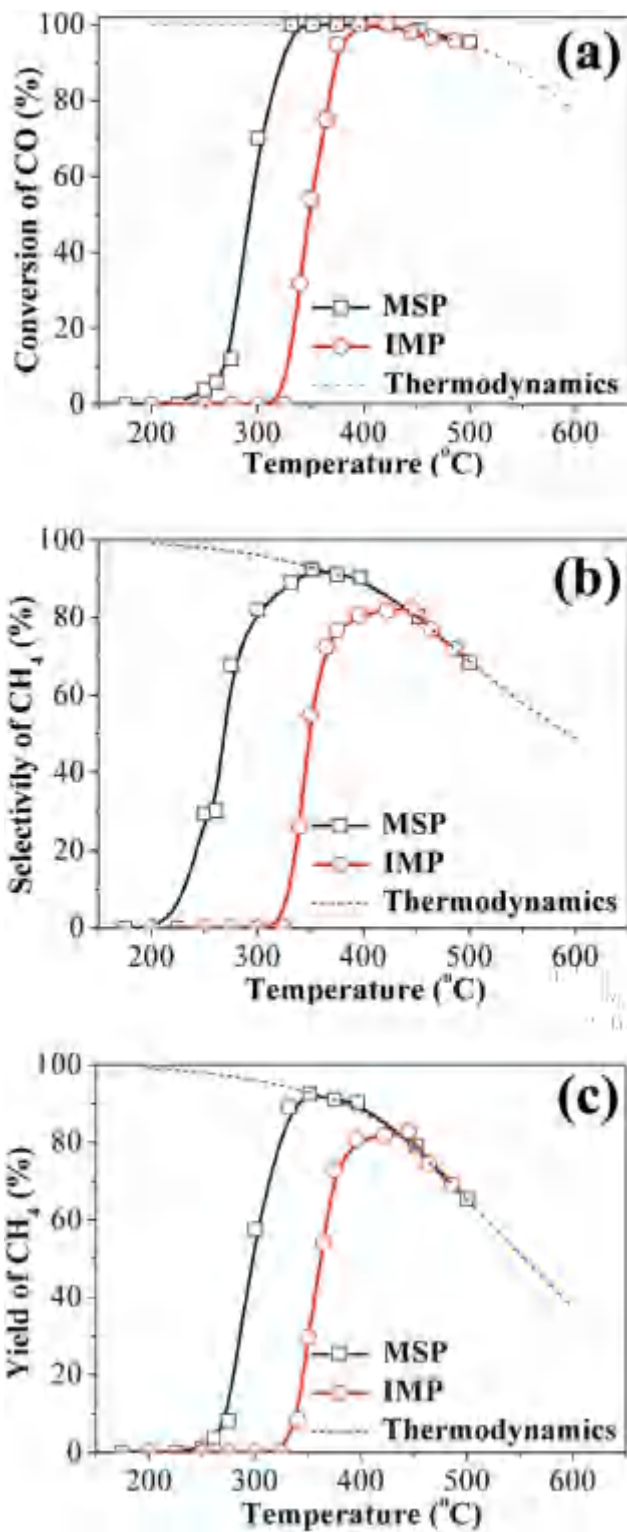


Figure 7. CO methanation of the hierarchical Ni/MgO catalyst (MSP) and impregnated Ni/MgO catalyst (IMP). (a) CO conversion, (b) selectivity of CH₄, and (c) yield of CH₄. [Color figure can be viewed at wileyonlinelibrary.com]

temperature was less than 300°C, both the CO conversion and selectivity of CH₄ were lower than the thermodynamic equilibrium values. This is because of the lower activity of catalyst

and partial conversion of CO to by-products such as CO₂ and carbon solids via a reversed methane-CO₂ re-forming reaction and the CO Boudouard reaction at low temperature.⁵⁶ Compared to the impregnated Ni/MgO catalyst (IMP), the selectivity and yield of CH₄ with the MSP catalyst were increased by

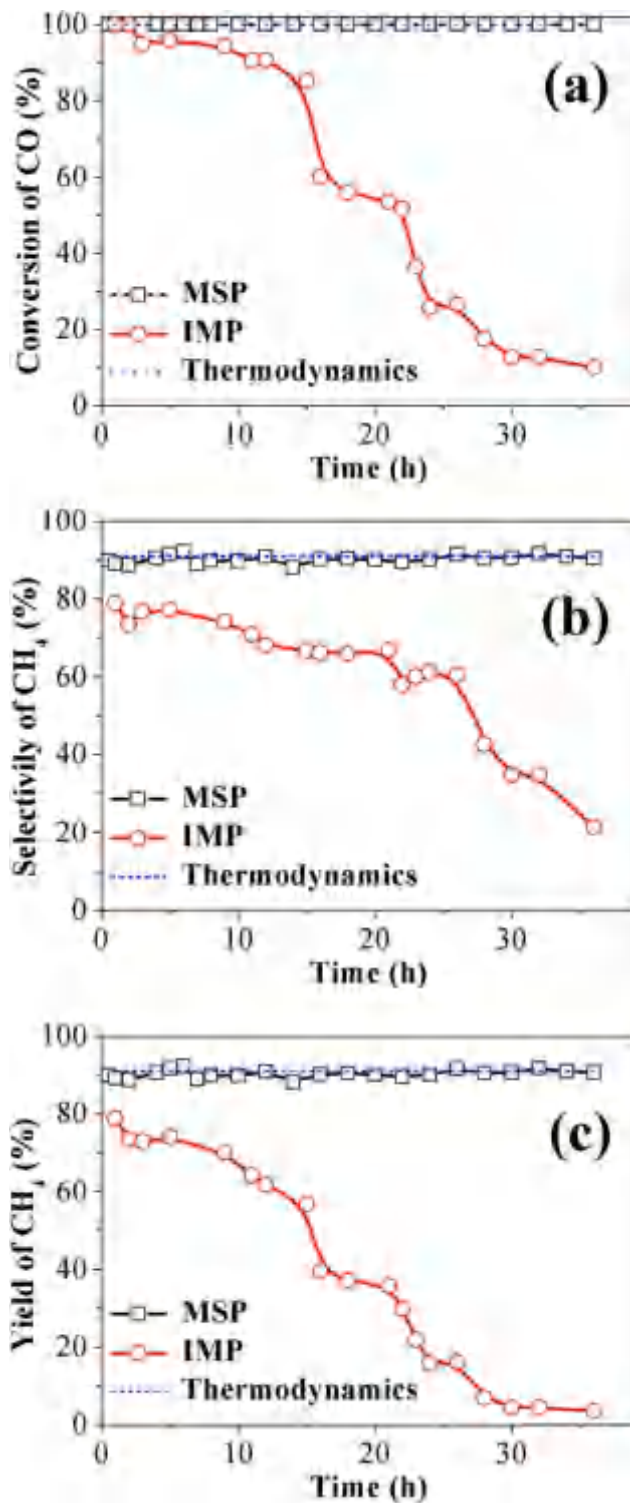


Figure 8. Stability tests of the hierarchical Ni/MgO (MSP) and impregnated Ni/MgO (IMP) catalysts during the CO methanation reaction. (a) CO conversion, (b) selectivity of CH₄, and (c) yield of CH₄. [Color figure can be viewed at wileyonlinelibrary.com]

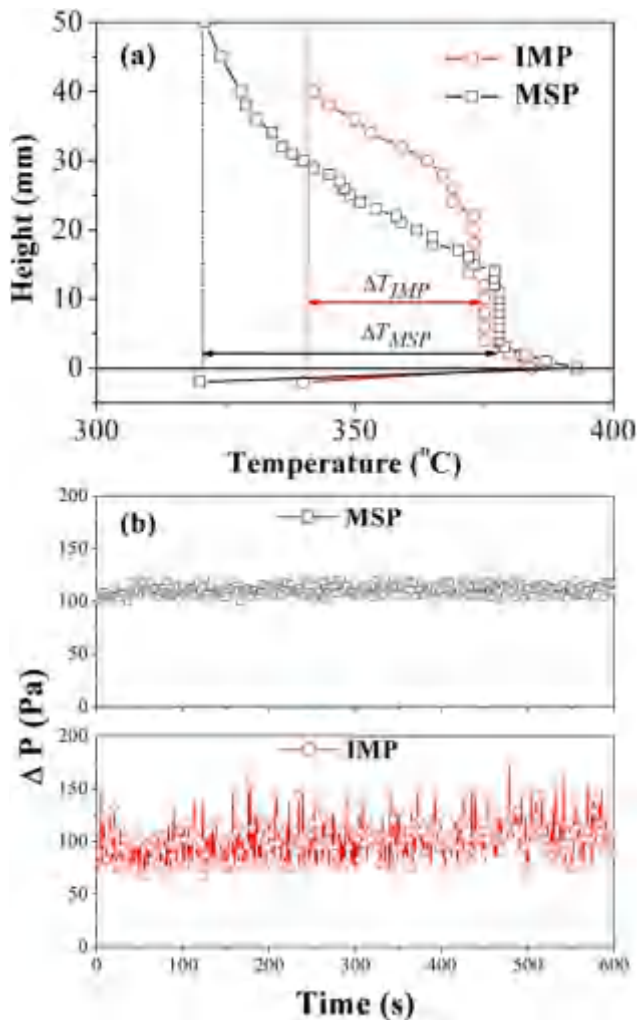


Figure 9. The axial temperature profiles (a) and bed pressure drop (b) over the MSP and IMP catalysts during the CO methanation reaction at 375°C in the fluidized-bed reactor.

[Color figure can be viewed at wileyonlinelibrary.com]

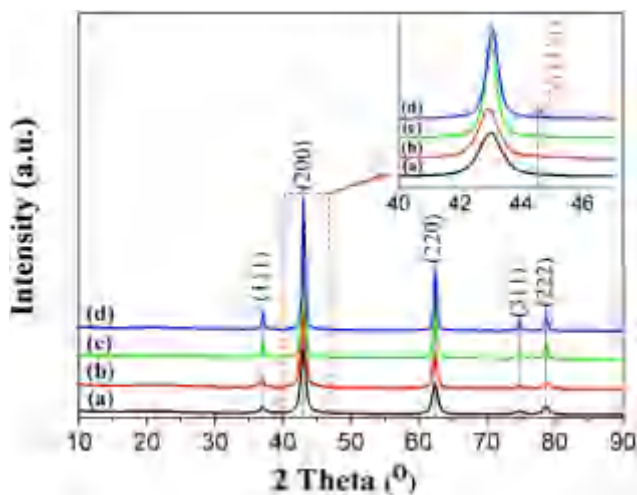


Figure 10. XRD patterns of the fresh MSP (a) and spent MSP (b), and the fresh IMP (c) and spent IMP (d) catalysts after the stability tests.

[Color figure can be viewed at wileyonlinelibrary.com]

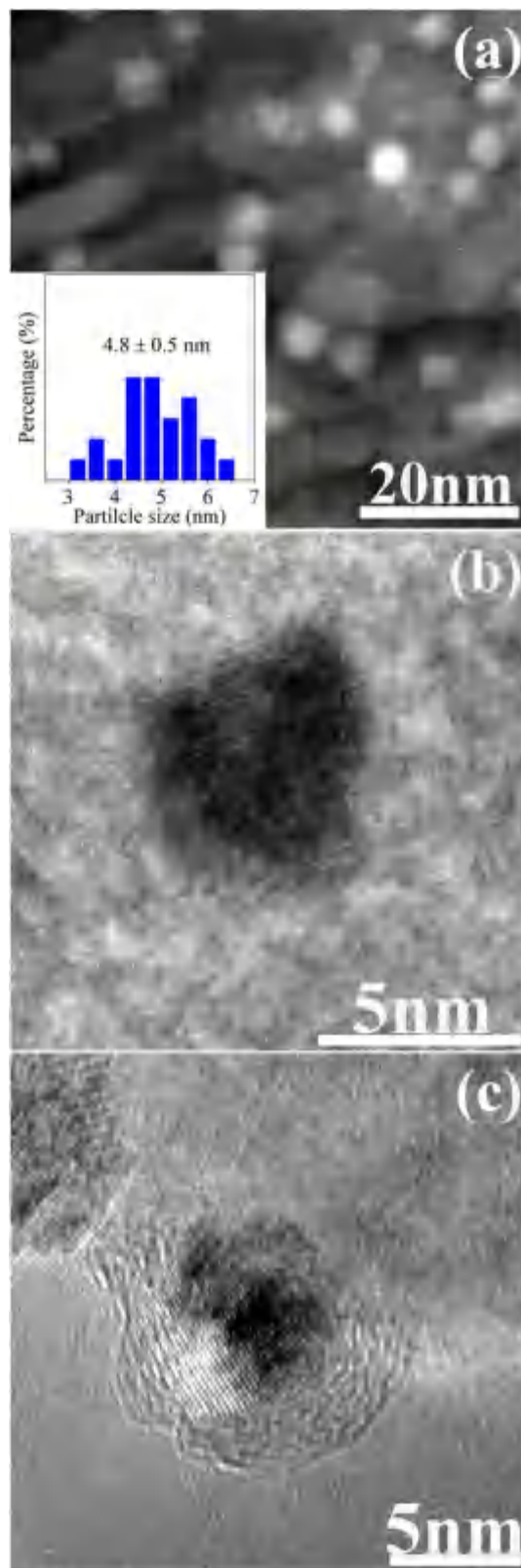


Figure 11. High-angle annular dark-field (HAADF)-STEM image (a), HRTEM image of the spent MSP (b), and spent IMP (c) catalysts after the stability tests.

The Inset in (a) is the particle size distribution of the spent MSP after the CO methanation stability test. [Color figure can be viewed at wileyonlinelibrary.com]

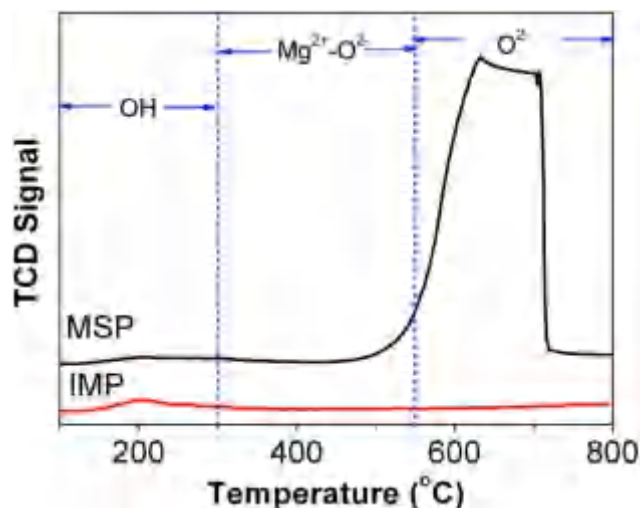


Figure 12. CO₂-TPD profiles of the MSP and IMP catalysts.

[Color figure can be viewed at wileyonlinelibrary.com]

8–15% (Figures 7b–c). Note that the MSP shows a light-off temperature of $\sim 80^\circ\text{C}$ lower than the IMP catalyst while delivering a higher CO conversion at or below 300°C .

The stability test results over the MSP and IMP catalysts are presented in Figure 8. The conversion of CO over the IMP catalyst is comparable to that over the MSP catalyst in the first 2 h at 375°C , but the selectivity and yield of CH₄ over the IMP

catalyst are much lower than those over the MSP catalyst. After the methanation reaction for 36 h at 375°C , the MSP catalyst still maintains a high CO conversion, high selectivity, and CH₄ yield. However, a dramatic decrease of the CO conversion, selectivity, and CH₄ yield are observed for the IMP catalyst, e.g., the CO conversion and CH₄ yield decrease to less than 10%, as illustrated in Figure 8. Compared with the IMP catalyst, the MSP catalyst shows much better catalytic activity and thermal stability. This enhancement is mainly attributed to the strong metal-support interactions, as evidenced from the H₂-TPR characterization.

Enhancement in CO methanation

The axial temperature profiles for the MSP and IMP catalysts are shown in Figure 9a. Good temperature control was confirmed in the fluidized-bed reactors for both MSP and IMP catalysts. The heights of the constant-temperature region, approximately 13 mm for the MSP catalyst and 21 mm for the IMP catalyst, are consistent with the height of the fluidized bed. As shown in Figure 9a, the furnace temperature was controlled at 320°C for the MSP catalyst and 340°C for the IMP catalyst. Large increases in the reaction temperature are observed for both catalysts due to the heat of the methanation reaction. The most striking differences are that the MSP catalyst shows a much higher increase of temperature than the IMP catalyst, indicating a higher selectivity of CH₄. The temperature slopes in Figure 9a indicate cooling due to heat transfer. According to the density and particle size of the catalysts, as shown in Table 1, both catalysts seem to belong to the

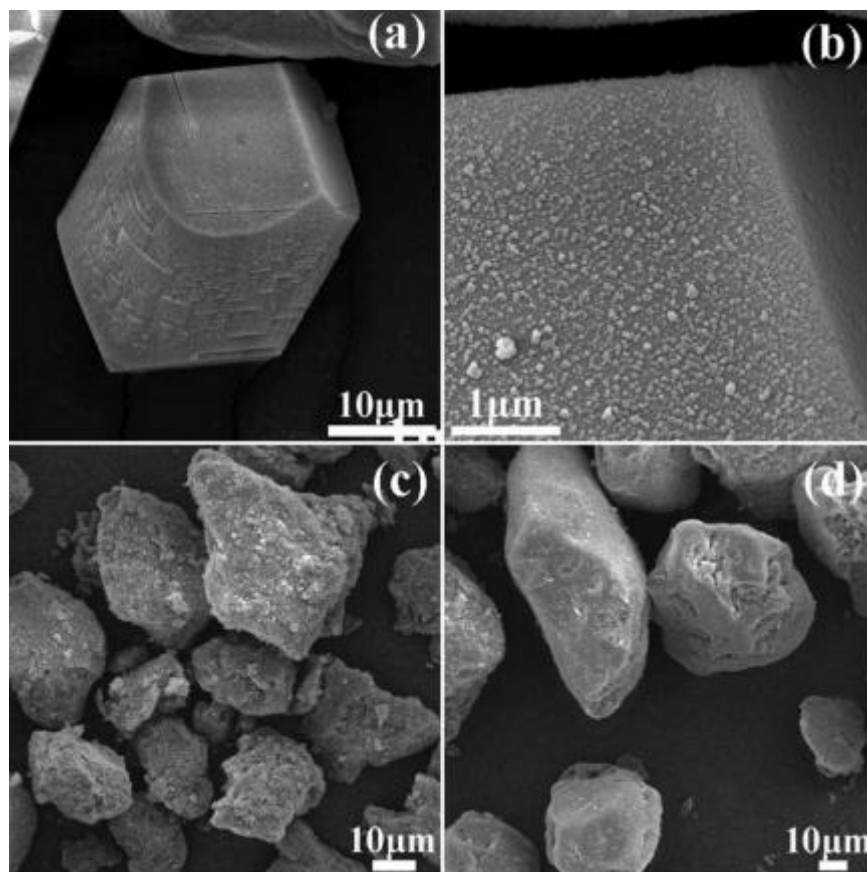


Figure 13. SEM images of the spent MSP catalyst (a) and its enlarged image (b), fresh IMP catalyst (c), and spent IMP catalysts (d).

Geldart A class of particles. As observed in Figure 9b, the MSP catalyst exhibits better fluidization quality than the IMP catalyst. This is suitable for avoiding the formation of hot spots in the fluidized-bed reactor, thus inducing less carbon deposition and higher selectivity of CH₄. The fluidized bed reactor used is too small to verify the effects of the fluidization quality of catalysts on heat transfer. At a large scale, these effects will play a more significant role in the removal of the heat of reaction.

Highly dispersed Ni particles can inhibit carbon deposition,⁵⁷ while these highly-dispersed Ni species are easy to agglomerate during the reaction.^{58,59} In this study, the spent catalysts after 36 h of CO methanation were characterized by XRD and TEM to investigate the changes in the crystal size of Ni in the MSP and IMP catalysts. The results show that both spent MSP and IMP catalysts exhibit very good crystallinity of MgO and no distinguishable Ni peaks (Figures 10a–d). This reveals that the Ni NPs may be supported on MgO in an amorphous or a highly-dispersed state.

The STEM image of the spent MSP catalyst shows that the average size of the crystalline Ni particles remains constant at 4.8 nm after the stability test (Figure 11a and inset in Figure 11a), indicating that Ni sintering can be neglected for MSP. The TEM image of the spent MSP catalyst shows that no carbon deposition is detected around the Ni NPs (Figure 11b). However, for the spent IMP catalyst, the Ni NPs are totally encapsulated by amorphous carbon after the stability test (Figure 11c), thereby completely deactivating the catalytic Ni sites. This severe carbon deposition on the Ni NPs is responsible for the deactivation of the IMP catalyst during long-term stability tests. Such carbon depositions are commonly reported for Ni catalysts subjected to steam re-forming above 700–1000°C.^{60,61}

In general, carbon deposition is closely related to the catalyst structure. Increased basicity of the support material promotes CO₂ chemisorption, which hinders the formation of deposited carbon via reverse CO disproportionation. The order of strength of the surface basic sites was determined to be the following: O²⁻ ions > oxygen in Mg²⁺-O²⁻ pairs > hydroxyl groups, corresponding to the three desorption temperature ranges in the CO₂-TPD profiles, viz. 550–750°C (strong basic sites), 300–550°C (medium basic sites), and 100–300°C (weak basic sites), respectively.⁶² CO₂-TPD measurements were carried out to study the basic strength and CO₂ adsorption capacity of the catalysts. As observed in Figure 12, the IMP catalyst shows the presence of weakly basic sites that can be assigned to the hydroxyl groups. Notably, the MSP catalyst exhibits a strong peak centered at 600°C, corresponding to oxygen vacancies. This indicates that the MSP catalyst abounds in surface oxygen and has a high oxygen storage capacity, which is of great importance for the dispersion of nickel metal and the inhibition of carbon deposition.^{63,64} The high surface oxygen mobility could help the activation of H₂O, promoting the water gas shift reaction and the oxidative removal of surface-bound carbon on nickel nano-clusters via the reverse CO disproportionation reaction, thus improving the selectivity and stability of the reaction.

In addition to carbon deposition and Ni sintering, attrition strength is another important property determining the utility of a catalyst in fluidized-bed reactors.⁶¹ The measured AI shown in Table 1 reveals that the MSP catalyst shows a lower AI than that of the IMP catalyst, indicating a higher attrition-resistance than that of the IMP catalyst. Compared to the

commercial c-Al₂O₃ powder used as a support for the FCC catalysts,⁶⁵ MSP also shows better attrition-resistance. From Figures 13a, b, the MSP catalyst exhibits a high wear-resistance, as no obvious change of the shape and edge are observed after the fluidized methanation tests. However, the surface of the IMP catalyst became quite smooth after 36 h of fluidized methanation (Figures 13c–d). Although attrition due to the rounding of edges might have a small contribution to the total deactivation of the IMP catalyst, this attrition will inevitably have a negative effect on the long-term stability.

Conclusions

We have developed a simple method to synthesize hierarchical Ni/MgO particles with high Ni dispersion and ordered mesopores via the guest-host chemistry exchange route. The hierarchical Ni/MgO particles show a very fine dispersion of Ni NPs and high surface oxygen mobility. The hierarchical Ni/MgO catalyst exhibits higher activity and stability for the CO methanation reaction compared to the catalyst synthesized by the conventional impregnation method. The enhancement in activity of the hierarchical Ni/MgO catalyst and its high resistance to coke-deposition are attributed to the multilayer structure that creates better metal-support interactions, high Ni dispersion to avoid sintering of Ni NPs, and high surface oxygen mobility that provides a high resistance to carbon deposition. The hierarchical Ni/MgO catalyst also shows good fluidization quality and a high attrition-resistance, making it suitable for efficient methanation in a fluidized-bed reactor. The proposed approach for improving catalytic activity by creating hierarchical Ni/MgO particles is encouraging in the context of designing novel catalysts for SNG production, from the perspective of matching the catalyst and the fluidized-bed reactor.

Acknowledgments

The work was supported by the National Natural Science Foundation of China (91334108 and U1462128), China National Fund for Distinguished Young Scientists (21325628), and the National Instrumentation Grant Program (2011YQ12003908).

Literature Cited

1. Shinde VM, Madras G. CO methanation toward the production of synthetic natural gas over highly active Ni/TiO₂ catalyst. *AIChE J.* 2014;60:1027–1035.
2. Kopyscinski J, Schildhauer TJ, Biollaz SMA. Production of synthetic natural gas (SNG) from coal and dry biomass—a technology review from 1950 to 2009. *Fuel* 2010;89:1763–1783.
3. Li S, Ji XZ, Zhang XS, Gao L, Jin HG. Coal to SNG: technical progress, modeling and system optimization through exergy analysis. *Appl Energ.* 2014;136:98–109.
4. Yu BY, Chien I-L. Design and economic evaluation of a coal-to-synthetic natural gas process. *Ind Eng Chem Res.* 2015;54:2339–2352.
5. Liu Z, Chu B, Zhai X, Jin Y, Cheng Y. Total methanation of syngas to synthetic natural gas over Ni catalyst in a microchannel reactor. *Fuel* 2012;95:599–605.
6. Rostrup-Nielsen J, Pedersen K, Sehested J. High temperature methanation: sintering and structure sensitivity. *Appl Catal A.* 2007;330:134–138.
7. Agnelli M, Kolb M, Mirodatos C. Co hydrogenation on a nickel catalyst. 1. Kinetics and modeling of a low-temperature sintering process. *J Catal.* 1994;148:9–21.
8. Mirodatos C, Pralraud H, Primet M. Deactivation of nickel-based catalysts during CO methanation and disproportionation. *J Catal.* 1987;107:275–287.

9. Li YK, Zhang QF, Chai RJ, Zhao GF, Liu Y, Lu Y, Cao FH. Ni-Al₂O₃/Ni-foam catalyst with enhanced heat transfer for hydrogenation of CO₂ to methane. *AIChE J.* 2015;61:1027–1035.
10. Schlesinger MD, Demeter JJ, Greyson M. Catalyst for producing methane from hydrogen and carbon monoxide. *Ind Eng Chem.* 1956; 48:68–70.
11. Cobb JJJ, Streeter RC. Evaluation of fluidized-bed methanation catalysts and reactor modeling. *Ind Eng Chem Proc Des Dev.* 1979;18: 672–679.
12. Lommerzhelm W, Flockenhaus C. One stage combined shift-conversion and partial methanation process for upgrading synthesis gas to pipeline quality. In: *Proceeding of tenth synthetic pipeline gas symposium*, Chicago, American Gas Association, 1978:439–451.
13. Seemann MC, Schildhauer TJ, Biollaz SMA. Fluidized bed methanation of wood-derived producer gas for the production of synthetic natural gas. *Ind Eng Chem Res.* 2010;49:7034–7038.
14. Schildhauer TJ, Biollaz SMA. Reactors for catalytic methanation in the conversion of biomass to synthetic natural gas (SNG). *Chimia* 2015;69:603–607.
15. Maurer S, Durán SR, Künstle M, Biollaz SMA. Influence of inter-particle forces on attrition and elutriation in bubbling fluidized beds. *Powder Technol.* 2016;291:473–486.
16. Kopyscinski J, Schildhauer TJ, Biollaz SMA. Employing catalyst fluidization to enable carbon management in the synthetic natural gas production from biomass. *Chem Eng Technol.* 2009;32:343–347.
17. Tada S, Minori D, Otsuka F, Kikuchia R, Osada K, Akiyama K, Satokawa S. Effect of Ru and Ni ratio on selective CO methanation over Ru–Ni/TiO₂. *Fuel* 2014;129:219–224.
18. Prieto G, Concepción P, Martínez A, Mendoza E. New insights into the role of the electronic properties of oxide promoters in Rh catalyzed selective synthesis of oxygenates from synthesis gas. *J Catal.* 2011;280:274–288.
19. Razaq R, Zhu HW, Jiang L, Muhammad U, Li CS, Zhang SJ. Catalytic methanation of CO and CO₂ in coke oven gas over Ni–Co/ZrO₂–CeO₂. *Ind Eng Chem Res.* 2013;52:2247–2256.
20. Zeng Y, Ma HF, Zhang HT, Ying WY, Fang DY. Highly efficient NiAl₂O₄-free Ni/c-Al₂O₃ catalysts prepared by solution combustion method for CO methanation. *Fuel* 2014;137:155–163.
21. Liu YJ, Gao JJ, Liu Q, Gu FN, Lu XP, Jia LH, Xu GW, Zhong ZY, Su FB. Preparation of high-surface-area Ni/a-Al₂O₃ catalysts for improved CO methanation. *RSC Adv.* 2015;5:7539–7546.
22. Tavares MT, Alstrup I, Bernardo CA, Rostrup-Nielsen JR. Carbon formation and CO methanation on silica-supported nickel and nickel–copper catalysts in CO + H₂ mixtures. *J Catal.* 1996;158:402–410.
23. da Silva DCD, Letichevsky S, Borges LEP, Appel LG. The Ni/ZrO₂ catalyst and the methanation of CO and CO₂. *Int J Hydrogen Energy.* 2012;37:8923–8928.
24. Yu Y, Jin GQ, Wang YY, Guo XY. Synthesis of natural gas from CO methanation over SiC supported Ni-Co bimetallic catalysts. *Catal Commun.* 2013;31:5–10.
25. Yin AX, Liu WC, Ke J, Zhu W, Gu J, Zhang YW, Yan CH. Ru nanocrystals with shape-dependent surface-enhanced Raman spectra and catalytic properties: controlled synthesis and DFT calculations. *J Am Chem Soc.* 2012;134:20479–20489.
26. Gao JJ, Jia CM, Zhang MJ, Gu FN, Xu GW, Su FB. Effect of nickel nanoparticle size in Ni/a-Al₂O₃ on CO methanation reaction for the production of synthetic natural gas. *Catal Sci Technol.* 2013;3:2009–2015.
27. van de Loosdrecht J, van der Kraan AM, van Dillen AJ, Geus JW. Metal-support interaction: Titania-supported and silica-supported Nickel catalysts. *J Catal.* 1997;170:217–226.
28. Fujita SI, Takezawa N. Difference in the selectivity of CO and CO₂ methanation reactions. *Chem Eng J.* 1997;68:63–68.
29. Gao JJ, Liu Q, Gu FN, Liu B, Zhong ZY, Su FB. Recent advances in methanation catalysts for the production of synthetic natural gas. *RSC Adv.* 2015;5:22759–22776.
30. Guo CL, Wu YY, Qin HY, Zhang JL. CO methanation over ZrO₂/Al₂O₃ supported Ni catalysts: a comprehensive study. *Fuel Process Technol.* 2014;124:61–69.
31. Zhang H, Dong YY, Fang WP, Lian YX. Effects of composite oxide supports on catalytic performance of Ni-based catalysts for CO methanation. *Chinese J Catal.* 2013;34:330–335.
32. Kester KB, Falconer JL. CO methanation on low-weight loading Ni/Al₂O₃: multiple reaction sites. *J Catal.* 1984;89:380–391.
33. Hu DC, Gao JJ, Ping Y, Jia LH, Gunawan P, Zhong ZY, Xu GW, Gu FN, Su FB. Enhanced investigation of CO methanation over Ni/Al₂O₃ catalysts for synthetic natural gas production. *Ind Eng Chem Res.* 2012;51:4875–4886.
34. Lebarbrier VM, Dagle RA, Albrecht KO, Li XH, Li LY, Taylor CE, Bao XH, Wang Y. Sorption-enhanced synthetic natural gas (SNG) production from syngas: a novel process combining CO methanation, water-gas shift, and CO₂ capture. *Appl Catal B Environ.* 2014;144:223–232.
35. Cai MD, Wen J, Chu W, Cheng XQ, Li ZJ. Methanation of carbon dioxide on Ni/ZrO₂–Al₂O₃ catalysts: effects of ZrO₂ promoter and preparation method of novel ZrO₂–Al₂O₃ carrier. *J Nat Gas Chem.* 2011;20:318–324.
36. Soo HS, Agiral A, Bachmeier A, Frei H. Visible Light-induced hole injection into rectifying molecular wires anchored on Co₃O₄ and SiO₂ nanoparticles. *J Am Chem Soc.* 2012;134:17104–17116.
37. Kim HY, Lee HM, Henkelman G. CO oxidation mechanism on CeO₂-supported Au nanoparticles. *J Am Chem Soc.* 2012;134:1560–1570.
38. Gross E, Liu JH, Alayoglu S, Marcus MA, Fakra SC, Toste FD, Somorjai GA. Asymmetric catalysis at the mesoscale: gold nanoclusters embedded in chiral self-assembled monolayer as heterogeneous catalyst for asymmetric reactions. *J Am Chem Soc.* 2013;135:3881–3886.
39. Wei SY, Wang Q, Zhu JH, Sun LY, Lin HF, Guo ZH. Multifunctional composite core–shell nanoparticles. *Nanoscale* 2011;3:4474–4502.
40. Wang YR, He QL, Ding KQ, Wei HG, Guo J, Wang Q, O’connor R, Huang XH, Luo ZP, Shen TD, Wei SY, Guo ZH. Multiwalled carbon nanotubes composited with palladium nanocatalysts for highly efficient ethanol oxidation. *J Electrochem Soc.* 2015;162:F755–F763.
41. Wang YR, He QL, Guo J, Wei HG, Ding KQ, Lin HF, Bhana S, Huang XH, Luo ZP, Shen TD, Wei SY, Guo ZH. Carboxyl multiwalled carbon-nanotube-stabilized palladium nanocatalysts toward improved methanol oxidation reaction. *ChemElectroChem.* 2015;2: 559–570.
42. Lu JL, Fu BS, Kung MC, Xiao GM, Elam JW, Kung HH, Stair PC. Coking- and sintering-resistant palladium catalysts achieved through atomic layer deposition. *Science* 2012;335:1205–1208.
43. Chen ZW, Waje M, Li WZ, Yan YS. Supportless Pt and PtPd nanotubes as electrocatalysts for oxygen-reduction reactions. *Angew Chem Int Ed.* 2007;46:4060–4063.
44. Andersson MP, Abild-Pedersen F, Remediakis IN, Bligaard T, Jones G, Engbæk J, Lytken O, Horch S, Nielsen JH, Sehested J, Rostrup-Nielsen JR, Nørskov JK, Chorkendorff I. Structure sensitivity of the methanation reaction: H₂-induced CO dissociation on nickel surfaces. *J Catal.* 2008;255:6–19.
45. Efstathiou AM. The CO/H₂ reaction on Rh/MgO studied by transient isotopic methods. *J Mol Catal.* 1991;67:229–249.
46. Takezawa N, Terumura H, Shimokawabe M, Kobayashi H. Methanation of carbon dioxide: preparation of Ni/MgO catalysts and their performance. *Appl Catal.* 1986;23:291–298.
47. Kai T, Furukawa M, Nakazato T, Tsutsui T, Mizuta K, Nakajima M. Analysis of fluidization quality of a fluidized bed with staged gas feed for reactions involving gas-volume reduction. *AIChE J.* 2010; 56:2297–2303.
48. Kai T, Toriyama K, Nishie K, Takahashi T, Nakajima M. Effect of volume decrease on fluidization quality of fluidized catalyst beds. *AIChE J.* 2006;52:3210–3215.
49. Kai T, Tsutsui T, Furusaki T. Features of fluidized catalyst beds for proper design and operation of catalytic reactions. *Ind Eng Chem Res.* 2004;43:5474–5482.
50. Sato K, Nagaoka K, Nishiguchi H, Takita Y. n-C₄H₁₀ autothermal reforming over MgO-supported base metal catalysts. *Int J Hydrogen Energy.* 2009;34:333–342.
51. Yoshida T, Tanaka T, Yoshida H, Funabiki T, Yoshida S. Study on the dispersion of nickel ions in the NiO–MgO system by X-ray absorption fine structure. *J Phys Chem.* 1996;100:2302–2309.
52. Arena FH, Cocke DL, Parmaliana A, Giordano N. Magnesia-supported nickel catalysts I. Factors affecting the structure and morphological properties. *J Catal.* 1991;132:58–67.
53. Parmaliana A, Arena F, Frusteri F, Coluccia S, Marchese L, Martra G, Chuvilin AL. Magnesia-supported nickel catalysts: II. Surface properties and reactivity in methane steam reforming. *J Catal.* 1993; 141:34–47.
54. Bond GC, Sarsam SP. Reduction of nickel/magnesia catalysts. *Appl Catal.* 1988;38:365–377.

55. Arena F, Liccardello A, Parmaliana A. The role of Ni²⁺ diffusion on the reducibility of NiO/MgO system: a combined TRP-XPS study. *Catal Lett.* 1990;6:139–150.
56. Gao JJ, Wang YL, Ping Y, Hu DC, Xu GW, Gu FN, Su FB. A thermodynamic analysis of methanation reactions of carbon oxides for the production of synthetic natural gas. *RSC Adv.* 2012;2:2358–2368.
57. Hou Z, Gao J, Guo J, Liang D, Lou H, Zheng X. Deactivation of Ni catalysts during methane autothermal reforming with CO₂ and O₂ in a fluidized-bed reactor. *J Catal.* 2007;250:331–341.
58. Sun N, Wen X, Wang F, Wei W, Sun Y. Effect of pore structure on Ni catalyst for CO₂ reforming of CH₄. *Energ Environ Sci.* 2010;3:366–369.
59. Barrientos J, Lualdi M, Boutonnet M, Järås S. Deactivation of supported nickel catalysts during CO methanation. *Appl Catal A.* 2014;486:143–149.
60. Tomishige K, Chen YG, Fujimoto K. Studies on carbon deposition in CO₂ reforming of CH₄ over nickel–magnesia solid solution catalysts. *J Catal.* 1999;181:91–103.
61. Zhang CX, Li SR, Li MS, Wang SP, Ma XB, Gong JL. Enhanced oxygen mobility and reactivity for ethanol steam reforming. *AIChE J.* 2012;58:516–525.
62. Puriwat J, Chaitree J, Suriye K, Dokjampa S, Praserttham P, Panpranot J. Elucidation of the basicity dependence of 1-butene isomerization on MgO/Mg(OH)₂ catalysts. *Catal Commun.* 2010;12:80–85.
63. Zhang CX, Li SR, Li MS, Wang SP, Ma XB, Gong JL. Enhanced oxygen mobility and reactivity for ethanol steam reforming. *AIChE J.* 2006;111:103–110.
64. Li SR, Gong JL. Strategies for improving the performance and stability of Ni-based catalysts for reforming reactions. *Chem Soc Rev.* 2014;43:7245–7256.
65. Cui DM, Liu J, Yu J, Su FB, Xu GW. Attrition-resistant Ni–Mg/Al₂O₃ catalyst for fluidized bed syngas methanation. *Catal Sci Technol.* 2015;5:3119–3129.

Manuscript received July 5, 2016, and revision received Sep. 28, 2016.